2026 IEEE International Conference on Robotics and Automation (ICRA 2026)
June 1-5, 2026. Vienna, Austria

Multistability Enabled Passive Multiplexing in an n-DOF, Underactuated Hyper-Redundant Robot

Cole Nagata[1], Jordan R. Raney[1] and Mark Yim[1]

Abstract— **New developments in robotics have allowed robots to become very small, and capable of completing tasks humans cannot. Current robots capable of achieving this are physically limited in how small they can be without compromising on other aspects such as sensing, strength, or complexity. Thus, we strive to understand how we can more compactly map complex mechanical outputs to a low number of mechanical inputs. This paper presents a novel design for a hyper-redundant robot, capable of passive multiplexing. This is achieved using bistable joints at each link, with each link having a different bistable moment in order to establish priority when multiplexing. In doing so, this simple mechanism is able to achieve individual joint control, and reach a variety of complex configurations. To demonstrate the proposed robot, we construct an eleven linked mechanism and four linked mechanism, in which we demonstrate multiplexing, as well as high positional accuracy. By simulating the mechanism, we also quantify a geometric relationship between individual links and the overall robot's workspace.**

I. INTRODUCTION

There are many robots for working in cluttered environments such as remote pipe inspection, surgical robots and machine inspection [1], [2], [3]. Two common types of robots in this category are continuum and hyper-redundant robots. Often inspired by biological systems like elephant trunks [4], octopus tentacles [5], or snakes [6], both continuum and hyper-redundant robots can be described as high aspect ratio robots that resemble a serial chain of 2D or 3D revolute joints. Continuum robots consist of an elastic structure that is deformed by actuators such as pneumatics or cables at the base of the robot, forming a smooth, curved structure designated as infinite Degrees of Freedom (DOF). Hyper-redundant robots are mechanically similar to serial robot arms, but instead contain many rigid links, with each link being very short and self contained.

Traditional serial robot arms often contain seven DOF in order to achieve a large dextrous workspace; however as obstacles are introduced, this dextrous workspace shrinks due to potential collisions. Continuum and hyper-redundant robots with many more DOF, achieve a larger dextrous workspace while in the presence of obstacles [7], [8], [4].

Both of these types of robots however also have fundamental limitations. Continuum robots, while being designated as having infinite DOF, have DOF that are often constrained due to underactuation, making the number of independent DOF proportional to the number of actuators controlling it. Typically robots have two to three sections, with each section able to achieve a different smooth curve shape [9], [10]. The natural elastic structure of continuum robots also means that they deform easily under loads, part of the reason why actuators are often kept at the base of continuum robots. Hyper-redundant robots who have individual joint control of a large or arbitrary number of degrees of freedom such as modular robots suffer from strength and space concerns, since the usual inclusion of a motor in each segment makes for heavier, bulkier links [11], [12]. This limits how small these robots can get, as well as how many links they can include, before the robot cannot support its own weight. Thus, there is a need for serial chain robots capable of higher articulation than continuum robots, and that are more miniaturizable and scalable than hyper-redundant and modular robots.

In this work, we propose a new type of serially linked hyper-redundant robot, which utilizes multistability enabled passive multiplexing to achieve complex curvatures, and n^2 unique configurations. Each link is bistable, meaning it can be at one of two angles when at rest, with the states of all of the links being driven by four tendons. The system is underactuated; any number of links can be driven by four cables, similar to a continuum robot. However by leveraging multistability the robot is able to perform passive multiplexing and adjust joints individually. In doing so, the proposed robot is highly articulated and contains no electronics within the links, making it lighter weight and easy to miniaturize.

A. Related Work

High DOF, serial chain robots are not new, with many variations of continuum robots and hyper redundant robots developed previously including tendon driven robots [13], [14], [15] which can wrap around objects but lack individual joint control. In digital electronics, time division multiplexing is the process of transmitting multiple digital signals over the same channel [16]. This strategy can also be applied to mechanisms. Cheng et al. utilized granular jamming to increase and decrease the stiffness of different sections of the robot to create multiplexing [17]. Bishop et al. proposed a shape memory alloy based clutch mechanism to lock cables in certain sections [18]. These solutions however require independent actuation mechanisms to act as mechanical switches for the demultiplexing process, limiting miniaturization and scaling poorly as the number of individual sections that are multiplexed increases.

Digital robots, which are robots whose actuators only have two stable states, are also related. Chirikjian et al. proposed a hyper-actuated, truss-based robots where each truss is a prismatic, bistable actuator such as a solenoid [19].

[1]Cole Nagata, Mark Yim, and Jordan Raney are with the Mechanical Engineering and Applied Mechanics Department, University of Pennsylvania, Philadelphia, PA, 19104 USA {cnagata, yim, raney} @seas.upenn.edu

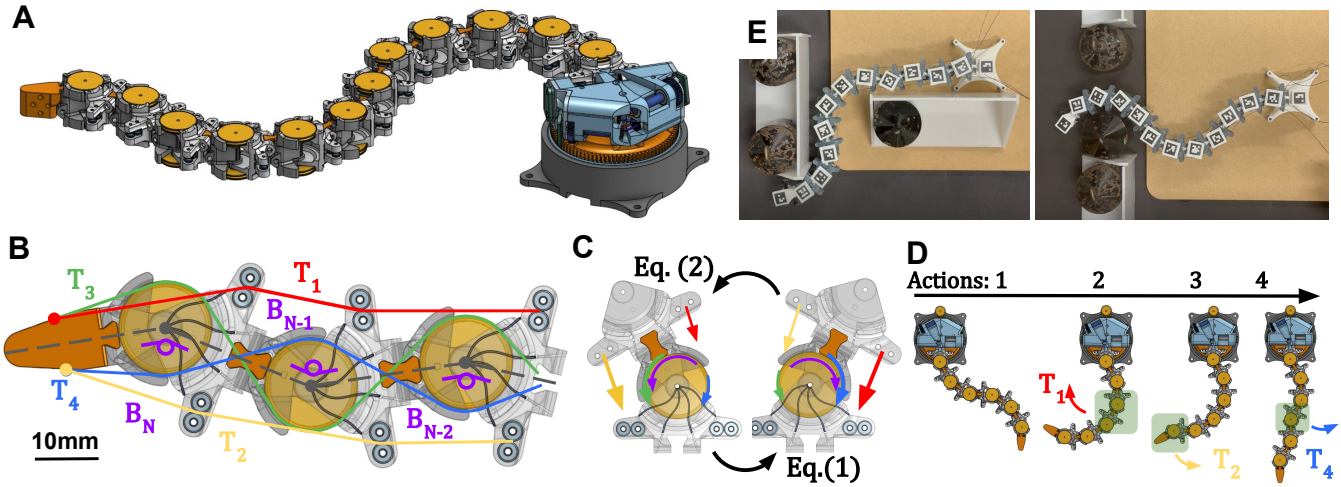

Fig. 1: Schematics showing the function of the proposed n-DOF, multi-stable robot. A: The overall design of the robot. B: Diagram of how the four tendons T_1, T_2, T_3, and T_4 are routed. C: The two states of a bistable module, and the forces and moments that determine its state. D: An example actuation strategy for moving from one state to another E: the mechanism navigates through tight areas.

Because this robot is hyper-actuated, the scaling of this mechanism becomes much more complex as the number of links increases, and due to the length restrictions of bistable prismatic joints the workspace is relatively small compared to the arm length [20]. Russo et al. utilized electromagnets to demonstrate a novel binary actuator capable of moving in 3D with high accuracy[21]. However doing so still requires n independent electromagnets for n independent states of the actuator, limiting miniaturization and scaling.

B. Overview

We seek to better understand the question: "How can we more compactly map complex mechanical outputs to a low number of mechanical inputs?" Being able to map a low number of inputs to a high number of outputs with as little hardware as possible is key to enabling highly scalable, high DOF serial robots. In this work, we have developed a novel n-DOF (large DOF), multi-stable underactuated hyper-redundant robot capable of achieving complex curvatures, and 2^n unique configurations, enabling it to navigate in constrained workspaces with very few actuators (Fig. 1). This is achieved by serially chaining bistable rotary joints, with each link containing a set of pulleys and tendons connecting through each link. Similar to a conventional cable driven continuum or hyper-redundant robot, pulling the tendons individually allows for the proposed robot to change shape; however the inclusion of bistable joints B_i acts as passive mechanical switches, performing the demuxing process based on the maximum bistable moment of the switch. Mechanical signals are transmitted via the applied tension in the four tendons, T_1, T_2, T_3, T_4. In order for the state of the joint, the moment applied by the tendons need to satisfy one the following inequalities, depending on which state it is in:

$$(M_{T_1} - M_{T_2}) + (M_{T_3} - M_{T_4}) > \max_{\theta}(M_{B_i}(\theta)) \quad (1)$$

$$(M_{T_1} - M_{T_2}) + (M_{T_3} - M_{T_4}) < -\max_{\theta}(M_{B_i}(\theta)) \quad (2)$$

By varying the maximum bistable moment of each joint, the joint with the lowest max bistable moment that satisfies the switching criteria changes states first, then the joint with the next lowest max bistable moment that satisfies the switching criteria, and so on. This establishes a predetermined demultiplexing order without the need for active components. By chaining multiple actuation signals together, more complex configurations can be reached. Because each link is driven by the same set of tendons, the number of actuators is thus highly scalable, with only the bistable moment increasing with the number of links. Furthermore, once tension is released from the tendons, the multi-stability of the links ensures that the robot maintains its shape. This allows the shape of the mechanism to continually change without needing to return to a neutral position, enabling it to achieve complex curvatures like a hyper redundant robot.

II. DESIGN

A. Bistable Mechanism

There are several important characteristics associated with the moment-angle behavior of the bistable beam: the angular range, the angle between two stable states θ, the maximum bistable moment M_{max}, and the angle θ_M at which the maximum bistable moment exists. θ affects the maximum curvature and workspace of the mechanism, while the maximum bistable moment designates which joints move

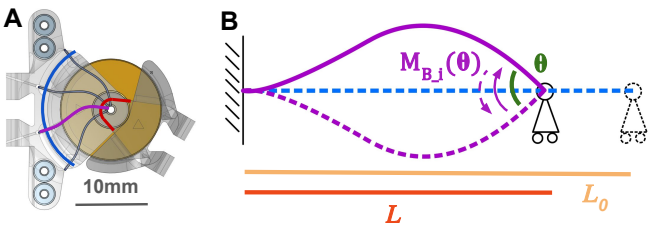

Fig. 2: A diagram of the proposed bistable mechanism A: embedded in the link. B: bistable beam model with original length L_0 and compressed span L. The beam's buckling modes (in purple) dictate the bistable states of the pivot.

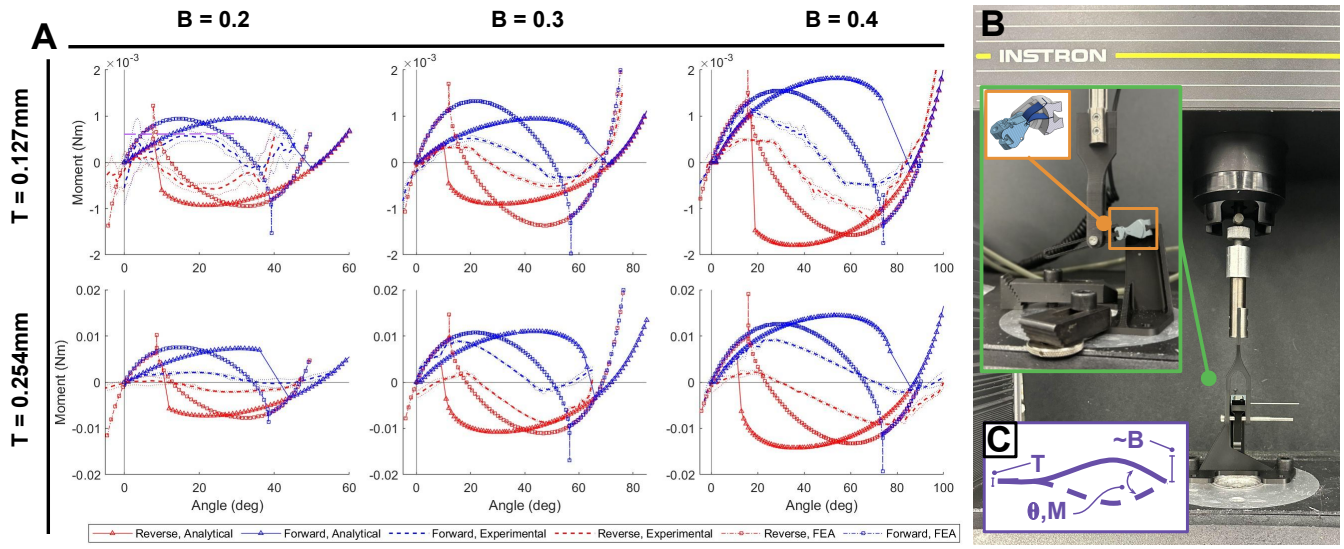

Fig. 3: Modeling the moment angle behavior of the bistable beam mechanism with different geometric parameters. A: Analytical model, numerical model, and experiments for six parameter sets, varying amplitude B and thickness T. The width of the beam is 7 mm, and the span of the buckled beam is 10 mm. B: Experimental setup, with bistable mechanism outlined in orange. C: diagram of parameters. model results differ slightly due to differences in boundary conditions.

first in the implementation of passive multiplexing. The last parameter θ_M is involved with multiplexing joints, as the closer θ_M is to 0, the less a given joint moves when it is not being multiplexed. This is a key part of what enables passive multiplexing to work, as each joint should ideally only move when the moment due to the tension in the cable is equal to the max moment, allowing only one joint to move at a time if all of the maximum moments are different.

In order to mechanically generate the bistable behavior in the rotary joints, we use a fixed-pinned buckled bistable beam mechanism (Fig. 2) [22]. The mechanism is created by connecting thin strips of laser cut polycarbonate to slits in a resin printed housing, and a spring steel shaft forms the pinned end of the buckled beams. By pre-compressing the beams during assembly, the beams buckle into the first buckling mode as depicted in Fig. 2. By applying a rotational moment to the rotary joint, the buckled beams snap from its initial buckling state to the opposite buckling state. The thickness, number of beams, and length of beams is varied in order to control the bistable moment and angle of the rotary joints.

In order to better understand the relationship between the listed parameters and the behavior of the mechanism, we start with an analytical model by using the Euler Bernoulli beam model of a fixed pinned beam subjected to compressive load P, and associated general solution [23].

$$EI\frac{d^4y}{dx^4} + P\frac{d^2y}{dx^2} = 0 \tag{3}$$

$$y(x) = A\cos(kx) + B\sin(kx) + Cx + D \tag{4}$$

We apply the boundary conditions of a fixed-pinned beam ($y(0) = y'(0) = y(L) = y''(L) = 0$) to the general solution to find a condition for k, where L is the compressed length of the beam.

$$\tan(kL) = kL \tag{5}$$

Solving for k gets us the following values, corresponding to the first, second and third buckling modes: $k_1L = 1.42\pi, k_2L = 2.46\pi, k_3L = 3.47\pi$. Next, we define the initial shape of the beam $y_0(x)$, and the arbitrary shape of the beam, $y(x)$ based on the first buckling mode, and the superposition of the first and second buckling mode plus an added error correction term, respectively [24],

$$\begin{aligned} y(x) = a_1(-k_1L\cos(k_1x) + \sin(k_1x) + k_1(L-x)) \\ +a_2(-k_2L\cos(k_2x) + \sin(k_2x) + k_2(L-x)) \\ +a_3(1-((L-2x)/L)^2)(x/L) \end{aligned} \tag{6}$$

$$y_0(x) = B(-k_1L\cos(k_1x) + \sin(k_1x) + k_1(L-x)) \tag{7}$$

where B is proportional to the amplitude of the beam. We calculate the constants associated with the arbitrary shape of the beam, a_1, a_2, and a_3 by solving for the minimum potential energy of the beam. We then calculate the total potential energy of the beam in terms of the bending energy U_B, work done by the applied moment U_M, and compressive energy U_C which can be expressed as,

$$U_{tot} = U_B + U_M + U_C \tag{8}$$

$$U_B = EI/2\int_0^L \left(\frac{d^2y}{dx^2}\right)^2 dx \tag{9}$$

$$U_M = -M\left(\frac{dy}{dx}(L_0)\right) \tag{10}$$

$$\begin{aligned} U_C &= \frac{Ebt(s-L_0)^2}{2L_0} \\ s &= \int_0^{L_0}\sqrt{1+\left(\frac{dy}{dx}\right)^2}dx \end{aligned} \tag{11}$$

where b is the width of the beam, t is the thickness of the beam, and M is the applied moment. By taking the derivative

of the total potential energy with respect to a_1, a_2, and a_3 and setting it to 0, we solve for constants and find the different possible solutions for the shape of the beam.

$$\begin{aligned} \frac{dU_{tot}(a_1,a_2,a_3)}{da_1} &= 0 \\ \frac{dU_{tot}(a_1,a_2,a_3)}{da_2} &= 0 \\ \frac{dU_{tot}(a_1,a_2,a_3)}{da_3} &= 0 \end{aligned} \tag{12}$$

These solutions are then filtered based on the angle and potential energy in order to find the actual solution.

We verify the analytical model using both a numerical model and physical tests. For the numerical model, we simulate the bistable beam using finite element analysis (Abaqus [25]). The beam is generated parametrically and assigned a fixed and radial boundary condition, where the geometry remains rigid for a short distance from the pivot but can still rotate. A radial boundary condition is used instead of a pinned one because the beam must be attached at the pinned end to actuate the rotary hinge, making the radial condition more accurate. The transition between stable states is simulated quasi-statically to distinguish between possible solutions near snap-through.

We then physically test the bistable behavior using a quasistatic materials testing machine (Instron 5564, 2.5 N load cell) and a jig that holds the rotary joint. The linear motion of the machine (60 mm/min) is converted to rotation through a pin-and-slot mechanism until the beam snaps from one buckling mode to the other. Tests are performed for different values of B ($B = 0.2, 0.3, 0.4$) to study how the initial shape affects the moment–angle behavior. Each beam has a 10 mm span, and two beams are tested simultaneously to reduce load-cell noise.

Comparing the analytical, numerical, and physical results in Fig. 3, all models show the same general trend: the moment increases with angle, becomes negative, then returns to zero, and the reverse path mirrors this behavior. This indicates bistability, with two equilibrium points—the zero-angle state and the maximum-angle state. All three models agree within 10° on the angular range, and the maximum moments are similar. Small differences arise mainly from how the membrane attaches to the housing: the analytical and numerical models use rigid connections, while the physical setup uses a transition fit that changes the boundary conditions. We also observe that the maximum moment in the numerical and physical models occurs nearer the initial state, while the analytical model predicts it closer to the next state; this difference results from using a pinned versus a radial boundary condition. The steeper moment curve near the initial state in the numerical and physical tests is beneficial, since it ensures that under cable tension, only one joint moves at a time.

The relationships between amplitude B, thickness T, and moment–angle behavior are also clear. Increasing B increases the angular range θ and the maximum moment, as a larger amplitude produces a longer, more stressed beam.

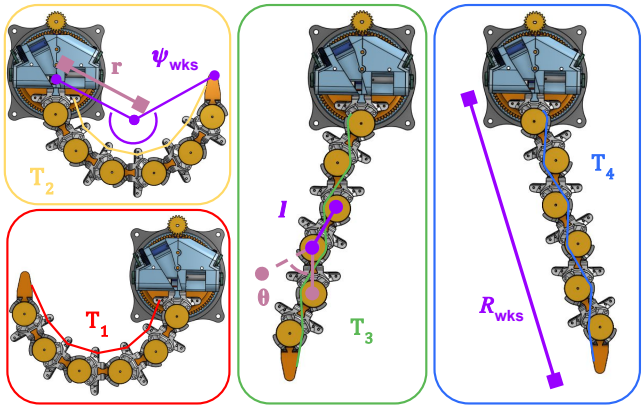

Fig. 4: Tendon routing of the bistable pivot joints for tendons T_1, T_2, T_3, and T_4. The end configuration of each tendon is depicted, and organized based on color. Tendons are driven by pulleys and motors in the circular base of the robot in light blue.

Increasing thickness raises the maximum moment while keeping the angular range unchanged, consistent with the cubic dependence of the second moment of area on thickness. These relationships allow us to tune the bistable joint's mechanical behavior so that passive multiplexing with many links is achievable.

B. Tendon Driven Actuation and Kinematics

In order to actuate the multistable, serially linked n-DOF structure, we can connect m tendons $T_i, \quad i = 1, \ldots, m$ to the end of the structure, and actuate them using pulleys at the base of the robot. When a given tendon is actuated, the resulting joint that changes first is the joint with the lowest maximum bistable moment that satisfies either Eq. (1) or Eq. (2), depending on the initial state of the joint. The resulting motion depends on the tendon routing geometry: the actuation direction is determined by the routing path, while the number of modules that switch depends on the total tendon displacement. For example, in Fig. 4 the four tendons are strung through different paths through the rotary joints via pulleys in each joint and connect to pulleys at the base of the robot. Of the four tendons, two are routed directly along the outside of the mechanism, and two snaked down the middle of the mechanism. Each tendon enables a distinct set of motions, with the outer tendons turning the joints all clockwise or counterclockwise, and the inner tendons alternating the direction in which each joint rotates between clockwise and counterclockwise.

We can more precisely express these states and actions through bitwise operations, where a given state of the mechanism S is represented as a n-bit binary vector, where the state of each joint is represented by a bit, being either 1 or 0, with the least significant bit representing the endmost joint and the most significant bit representing the joint closest to the base. We can also express the state reached by fully actuating a given tendon T_i as $S_{end,i}$, which would also be a n bit binary vector. In order to implement forward kinematics, we can introduce the following equation:

$$S_{t+1} = S_t \oplus \delta(S_t \oplus S_{end,i}, \Delta l_i) \tag{13}$$

where the function δ outputs a n bit binary vector whose 1 bits indicate the bits that will change from time t to $t+1$, based on the change in length of tendon T_i, Δl_i and the bits that can change, $S \oplus S_{end,i}$, where $\oplus$ is the logic XOR operator. In order to convert from state S_t to cartesian coordinates r_i, we can use the following geometric equation:

$$r_i = r_{i-1} + l \begin{bmatrix} cos(\phi_i) \\ sin(\phi_i) \\ 0 \end{bmatrix}, \phi = T_b^I[\theta_{range}(S_t - \frac{1}{2})] \quad (14)$$

where ϕ is a n-dimensional vector representing the link orientations in the inertial frame, and T_b^I maps the joint angles in the body frame to the inertial frame.

Due to the unique actuation strategy and high number of possible degrees of freedom, inverse kinematics for the proposed digital hyper-redundant mechanism offers a unique set of challenges. We can move from arbitrary states S_t to S_{des} quite easily by recursively changing the lowest prioritized bits that do not match those of S_{des} until S_t equals S_{des}, which has a time complexity of $O(n)$. However when searching for the desired configuration S_{des}, The configuration space contains 2^n discrete states, making brute force exploration and other traditional methods perform poorly as the number of joints increases. Lees et al. proposed a combinatorial approach that allows for no more than k actuators to be changed at a time, making the time complexity of path planning $O(n^k)$ [26]. Ebert-Uphoff et al. proposed a tree search algorithm and uses a workspace density metric in order to maximize the redundancy remaining to reach the goal with $O(n)$ complexity [27]. However, because of the fixed sequential ordering of the mechanism the system is not commutative, meaning actuating two different tendons can result in two different end configurations depending on the order in which the actions are carried out. We can take advantage of this by taking a similar approach to [26] by limiting our search to configurations that actuate only one of the m different tendons, which reduces the search space to mn, or $O(mn)$. If we want to sequentially actuate only k of the m actuators, the search space becomes $(mn)(mn-1)^{k-1} \sim (mn)^k$, so searching this has a polynomial time complexity of $O(m^k n^k)$ for large values of n. Thus for $k \ll n$, the scaling of search methods improves drastically.

III. EXPERIMENTS

A. Workspace and Scaling

By adjusting robot design parameters such as link length and number of joints, both the workspace and its spatial density can change significantly. To characterize these effects, we relate the geometric parameters of each link, θ and l, to two global workspace parameters: R_{wks}, the outer workspace radius, and ψ_{wks}, the robot's maximum wrap angle. These quantities describe the reachable region of the mechanism. A wrap angle $\psi < 2\pi$ limits the robot from curling inward toward its center, while $\psi > 2\pi$ allows higher curvature but requires an over-wrapping constraint to avoid self-collision. The number of links also affects the workspace, as more

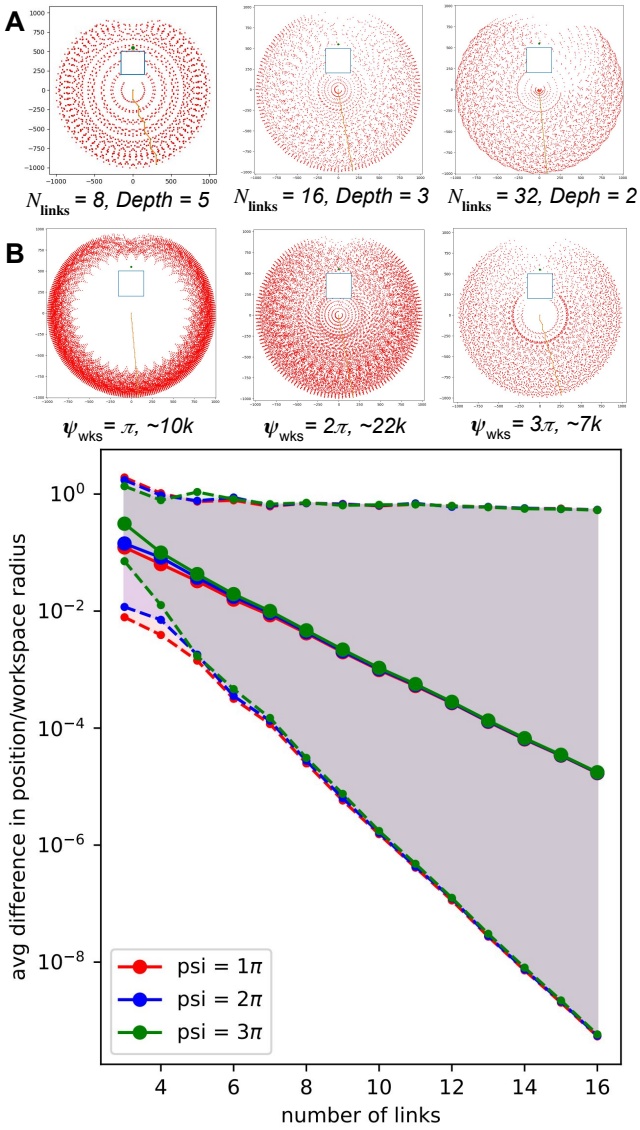

Fig. 5: Simulated results relating the robot's workspace area (in mm) and geometric parameters max wrap angle ψ_{wks}, number of links N_{links}. A: Spatial density of the workspace (in mm) increases as the number of links increases, number of points increases then decreases. B: the workspace has an inner radius if $\psi_{wks} < 2\pi$ but is more sparsely populated if $\psi_{wks} > 2\pi$. The number of actions needed to reach a given point decreases with the number of links.

joints increase the number of distinct configurations and thus the spatial density. The parameters are related through:

$$\psi_{wks} = N \arcsin\left[\frac{l}{r}\cos\left(\frac{\theta}{4}\right)\right] \quad (15)$$

$$R_{wks} = \begin{cases} l\sqrt{\sin^2\left(\frac{\theta}{4}\right) + \cos^2\left(\frac{\theta}{4}\right)N^2} & \text{if N is odd} \\ l\cos\left(\frac{\theta}{4}\right)N & \text{if N is even} \end{cases} \quad (16)$$

We evaluate the impact of these parameters by simulating the robot's workspace (Python). Given its discrete nature, its workspace can be mapped to a graph of its configuration

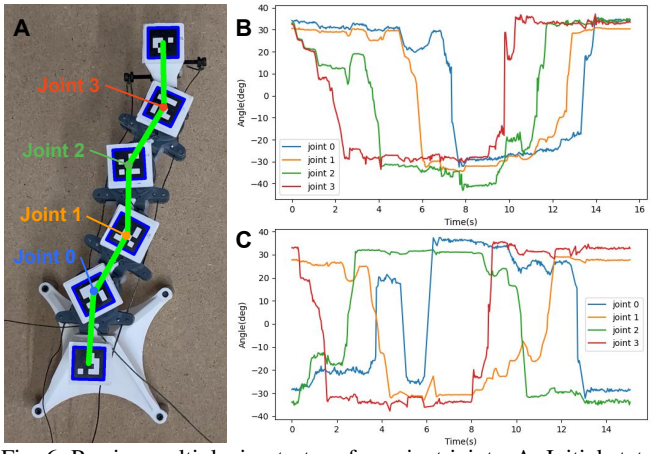

Fig. 6: Passive multiplexing test on four pivot joints. A: Initial state of plot C, with AprilTags detected. B: plot of angle of each pivot joint with respect to time when moving from curled to the right to curled to the left, then back to the right. C: plot of angle of each pivot joint with respect to time when moving from zig zagging to the right to zig zagging to the left. during both tests, tendons were operated by hand, and tension released after every joint change.

space, where each node is a different configuration, and vertices are the different actions possible by actuating the different tendons. An obstacle is included in the workspace in order to assess its ability to reach areas otherwise difficult for traditional serial manipulators to reach. The primary parameters that are varied are ψ (π, 2π, 3π), and the number of links N $(8, 16, 32)$. The simulation was limited by the number of vertices in the graph that are traversed (5, 3, 2).

As seen in Fig. 5, the workspace has a clear relationship between ψ and N, with the number of links being logarithmically related to the normalized discrete distance between positions, and the workspace having an inner radius when $\psi < 2\pi$. By increasing the number of links, not only are there exponentially more distinct, discrete configurations, but by keeping the reach constant the link length l and angular range theta decreases, decreasing the distance the end effector moves when a single link is changed. Because of this the workspace spatial density is also unaffected by ψ. As the number of links increases, the number of vertices needed to traverse to a given point decreases. This may seem counter intuitive since having more joints means more DOF to control. However by having more links, the number of links that can change when a single tendon is actuated increases, creating more possible configurations achievable from actuating a single tendon.

When controlling the number of vertices traversed, the spatial density of the workspace changes with respect to N, as well as now ψ, with $\psi > 2\pi$ having a lower spatial density. This is due to the possibility of self collision when $\psi > 2\pi$, limiting the number of vertices from a given configuration. As a result, while the spatial density is independent of ψ, the amount of vertices traversed to reach a given point is higher for larger values of ψ.

B. Passive Multiplexing

To validate the performance of the mechanism, we tested both the bistable enabled passive multiplexing and the positional accuracy of the mechanism. We assembled four bistable rotary joints in series. Each bistable module has a different bistable moment (τ_3 = 1 N mm, τ_2 = 2 N mm, τ_1 = 3 N mm, τ_0 = 4 N mm) in order to enable the rotary joints to actuate non-uniformly, with the lowest actuating first. Next, the joints were attached to a test stand, and the tendons actuated manually to move the joints. This test is run for both the outer and inner sets of tendons. In each test one of the tendons is pulled until the end configuration is reached, then pulled by the opposing tendon back to its original position. The tendons are pulled slowly enough to ensure there are no inertial effects, and the position of each joint is tracked using Apriltags connected to every joint [28].

As seen in Fig. 6, both tests indicate that the use of bistable joints enables passive multiplexing, with both tests showing the joints changing one at a time, and staying near $\pm$30 degrees when idle. During both tests, any joint that would later move shifted by $\sim 10^\circ$ while other joints were moving, since the moment due to the tendon is applied at all joints. In the test of the inner tendons, joint 0 shifts close to the +30 position around 4 seconds, when joint 1 is supposed to be multiplexed, and then drops back to -30. This is due to increased friction on the inner tendons due to their zig-zagging path, which causes a higher loss in tension between joint 0 and joint 1; however as tension is released when joint 1 finishes moving, joint 0 returns to its original equilibrium position due to the applied moment of the bistable mechanism.

C. Positional Accuracy

We tested the positional accuracy of the mechanism by actuating the mechanism into different distinct positions and characterizing the error between the desired and actual position of each joint. This was achieved by assembling 11 bistable rotary joints in series. Similar to the previous experiment, each bistable module has a different bistable moment (τ_{10} = 1 N mm, τ_9 = 2 N mm, τ_8 = 3 N mm, τ_7 = 4 N mm, τ_6 = 10 N mm, τ_5 = 15 N mm, τ_4 = 20 N mm, τ_3 = 25 N mm, τ_2 = 30 N mm , τ_1 = 35 N mm, and τ_0 = 40 N mm). These moments were chosen in order to minimize the largest moment, while still being able to switch joints individually in the proper order. Eight different configurations were chosen to be tested for accuracy (four for the end configurations of each tendon, and four random configurations), and each configuration was tested four times. During each test. The configuration of the mechanism was recorded using AprilTags connected to each joint, which was then compared to the ideal behavior shape, where the joints are at either positive or negative 30 degrees. From this, we calculate both the error for every joint with respect to the predicted configuration, and the standard deviation between tests.

As shown in Fig. 7, the error between the predicted and real joint position grows linearly with the joint num-

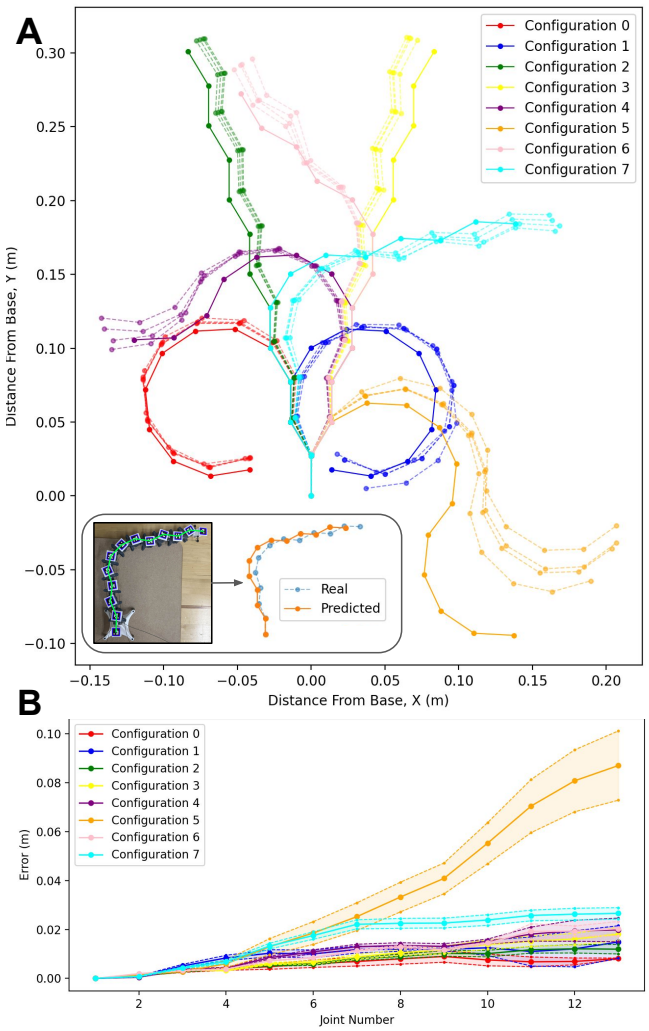

Fig. 7: Positional accuracy for an eleven jointed mechanism. A: all configurations tested, with the predicted configuration in solid lines and actual configuration in dashed lines. B: average error and standard deviation of error between the predicted and real joint locations versus joint number across all configurations and tests.

ber. Slight changes in angle at joints closer to the base of the mechanism cause larger displacements for points further away from the pivot point (i.e., at the end of the mechanism). We also notice that in most configurations the standard deviation of error across different tests is an order of magnitude smaller than the average error. This seems to indicate that the mechanism is more precise than accurate, and that the positional error is more likely due to slight differences between the predicted angular range θ of the bistable mechanism and the actual angular range θ. This is also visible in the plot of all the different configurations tested. Additionally, the standard deviation is much higher for joints 10-13 when compared to joints 1-9. This is likely attributed to the change in bistable membrane thickness, since based off of our previous characterization, achieving a bistable moment in the 1 N mm-5 N mm range means the bistable membrane needs to be thinner than those in the 10 N mm-40 N mm range, increasing the relative error.

IV. DISCUSSION

While the design of the mechanism allows for an arbitrarily large number of links, in practice there are practical limits that limit the number. For our implementation, we achieved a maximum of 11 links, with more than this resulting in joints not actuating in the proper order. This is due to two main factors: friction and the moment range. Friction has a large impact on joint movement due to the change in angle the tendons experience when passing through each joint resulting in a loss in tension. This primarily affects the two middle tendons, since they experience the highest change of angle in each joint, ranging between $38°$ and $98°$. We can approximate the loss in tension for the i^{th} link T_i based on the capstan equation or a simplified coulomb friction model dependent on whether the tendon is slipping on the pulley or the pulley slipping on the axle, respectively.

$$T_i = T_{applied} e^{-\mu\varphi i} \tag{17}$$

$$T_i = T_{applied} \left(\frac{r + r_a \mu_a \sin(\frac{\varphi}{2})}{r - r_a \mu_a \sin(\frac{\varphi}{2})} \right)^{-i} \tag{18}$$

Where r is the radius of the pulley, r_a is the radius of the axle, μ is the coefficent of friction between the tendon and the pulley, μ_a is the coefficient of friction between the pulley and the axle, and φ is the wrap angle of the tendon around the pulley. Based on both of these equations the tension approaches 0 as the number of links increases, creating a limit to how many links can be added as the endmost link needs enough tension to be able to switch states. This is all proportional to the tension applied, however, meaning that if the bistable moment of the joints closer to the base is higher than the moment generated by the applied tension required in order to reach the resulting tension at the end, then the joints will actuate in proper order. This means that the maximum number of achievable joints is based on both the rate of decay in friction and the range of achievable moments. We can more precisely describe this with the following inequalities:

$$\max_{\theta}(M_{B_i}(\theta)) > \max_{\theta}(M_{B_{i+1}}(\theta))\gamma \tag{19}$$

$$\max_{\theta}(M_{B_n}(\theta)) > \max_{\theta}(M_{B_0}(\theta))\gamma^n \tag{20}$$

$$\gamma = \begin{cases} e^{\mu\varphi} & \text{if tendon slips} \\ \left(\frac{r+r_a\mu_a \sin(\frac{\varphi}{2})}{r-r_a\mu_a \sin(\frac{\varphi}{2})}\right) & \text{if pulley slips} \end{cases} \tag{21}$$

where (15) refers to the moment relationship between the max moment two neighboring joints, (16) refers to the moment range, and γ is the rate of decay based on (13) and (14). We also express both as inequalities to ensure that joints are actuated sequentially.

Based on the stated inequalities, we know that the moment range is a limiting factor in how many links can be added. For our implementation, the minimum and maximum moments are 1 N mm and 40 N mm. The current design of the bistable mechanism is limited in the max number of membranes that can be added and how thick they can be, since the membranes

need to be spaced apart to avoid self-collision. Because this design only uses two thicknesses of polycarbonate and a maximum four membranes per module, the range in resulting moments is limited. This, compounded with the effects of friction, results in a maximum of 11 links. Because most of these restrictions are material-based, improvements on the number of possible links can be made by changing materials, and/or using multiple materials to have a wider range of elastic moduli for the membranes, and lower friction in the pulleys.

V. CONCLUSIONS AND FUTURE WORK

In this paper, we have proposed, characterized, and validated a novel multistable hyper-redundant robot, capable of passive multiplexing. This is possible due to the use of bistable pivot joints that use a polycarbonate membrane to generate the bistable effect. By varying the bistable moment of the different pivot joints, we establish a priority in which joint should move first. This enables the robot to perform more complex shape change, including contouring around different surfaces, grasping objects, and navigating around cluttered areas. The system also has the potential to be extremely miniaturizable, with no electrical components on the links meaning that the only thing that needs to be shrunk is the bistable mechanism, whose only moving part is the pivot point.

While this work focuses primarily on the design of the mechanism, there is a lot of potential future work on this mechanism in order to better control and understand it. Given its complex dynamics and multistable nature, common control methods become complicated and any Jacobian based path planning does not work, offering a unique problem in order to optimally control it. Additionally, further work on characterizing and improving the tension decay and bistable moment range of the links is important to increasing the possible number of links.

REFERENCES

[1] D. Rollinson and H. Choset, "Pipe network locomotion with a snake robot," *Journal of Field Robotics*, vol. 33, no. 3, pp. 322–336, 2016.

[2] J. Burgner-Kahrs, D. C. Rucker, and H. Choset, "Continuum robots for medical applications: A survey," *IEEE Transactions on Robotics*, vol. 31, no. 6, pp. 1261–1280, 2015.

[3] I. D. Walker, H. Choset, and G. S. Chirikjian, *Springer Handbook of Robotics*. Springer, 2008.

[4] I. D. Walker and M. W. Hannan, "A novel'elephant's trunk'robot," in *1999 IEEE/ASME International Conference on Advanced Intelligent Mechatronics (Cat. No. 99TH8399)*. IEEE, 1999, pp. 410–415.

[5] M. Cianchetti, M. Calisti, L. Margheri, M. Kuba, and C. Laschi, "Bioinspired locomotion and grasping in water: the soft eight-arm octopus robot," *Bioinspiration & biomimetics*, vol. 10, no. 3, p. 035003, 2015.

[6] C. Wright, A. Buchan, B. Brown, J. Geist, M. Schwerin, D. Rollinson, M. Tesch, and H. Choset, "Design and architecture of the unified modular snake robot," in *2012 IEEE International Conference on Robotics and Automation*, 2012, pp. 4347–4354.

[7] G. S. Chirikjian and J. W. Burdick, "Hyper-redundant robot mechanisms and their applications," *Algorithms*, vol. 1, no. 9, p. 10, 1991.

[8] A. Degani, H. Choset, A. Wolf, and M. Zenati, "Highly articulated robotic probe for minimally invasive surgery," in *Proceedings 2006 IEEE International Conference on Robotics and Automation, 2006. ICRA 2006.*, 2006, pp. 4167–4172.

[9] E. Amanov, T.-D. Nguyen, and J. Burgner-Kahrs, "Tendon-driven continuum robots with extensible sections—a model-based evaluation of path-following motions," *The International Journal of Robotics Research*, vol. 40, no. 1, pp. 7–23, 2021.

[10] W. McMahan, B. A. Jones, and I. D. Walker, "Design and implementation of a multi-section continuum robot: Air-octor," in *2005 IEEE/RSJ International Conference on Intelligent Robots and Systems*. IEEE, 2005, pp. 2578–2585.

[11] M. Yim, D. Duff, and K. Roufas, "Polybot: a modular reconfigurable robot," in *Proceedings 2000 ICRA. Millennium Conference. IEEE International Conference on Robotics and Automation. Symposia Proceedings (Cat. No.00CH37065)*, vol. 1, 2000, pp. 514–520 vol.1.

[12] C. Liu, Q. Lin, H. Kim, and M. Yim, "Smores-ep, a modular robot with parallel self-assembly," *Autonomous Robots*, vol. 47, no. 2, pp. 211–228, 2023.

[13] S. Hirose and H. Yamada, "Snake-like robots [tutorial]," *IEEE Robotics & Automation Magazine*, vol. 16, no. 1, pp. 88–98, 2009.

[14] M. Russo, S. M. H. Sadati, X. Dong, A. Mohammad, I. D. Walker, C. Bergeles, K. Xu, and D. A. Axinte, "Continuum robots: An overview," *Advanced Intelligent Systems*, vol. 5, no. 5, p. 2200367, 2023.

[15] Z. Wang, N. M. Freris, and X. Wei, "Spirobs: Logarithmic spiral-shaped robots for versatile grasping across scales," *Device*, vol. 3, no. 4, p. 100646, 2025. [Online]. Available: https://www.sciencedirect.com/science/article/pii/S2666998624006033

[16] W. Stallings, *Data and computer communications*. Pearson Education India, 2007.

[17] N. G. Cheng, M. B. Lobovsky, S. J. Keating, A. M. Setapen, K. I. Gero, A. E. Hosoi, and K. D. Iagnemma, "Design and analysis of a robust, low-cost, highly articulated manipulator enabled by jamming of granular media," in *2012 IEEE international conference on robotics and automation*. IEEE, 2012, pp. 4328–4333.

[18] C. Bishop, M. Russo, X. Dong, and D. Axinte, "A novel underactuated continuum robot with shape memory alloy clutches," *IEEE/ASME Transactions on Mechatronics*, vol. 27, no. 6, pp. 5339–5350, 2022.

[19] G. S. Chirikjian, "A binary paradigm for robotic manipulators," in *Proceedings of the 1994 IEEE International Conference on Robotics and Automation*. IEEE, 1994, pp. 3063–3069.

[20] I. Ebert-uphoff and G. S. Chirikjian, "Efficient workspace generation for binary manipulators with many actuators," *Journal of Robotic Systems*, vol. 12, no. 6, pp. 383–400, 1995. [Online]. Available: https://onlinelibrary.wiley.com/doi/abs/10.1002/rob.4620120605

[21] M. Russo, J. Barrientos-Diez, and D. Axinte, "A kinematic coupling mechanism with binary electromagnetic actuators for high-precision positioning," *IEEE/ASME Transactions on Mechatronics*, vol. 27, no. 2, pp. 892–903, 2022.

[22] D. Pan, Y. Xu, W. Li, and Z. Wu, "Novel rotational motion actuated beam-type multistable metastructures," *Materials & Design*, vol. 224, p. 111309, 2022. [Online]. Available: https://www.sciencedirect.com/science/article/pii/S0264127522009315

[23] O. A. Bauchau and J. I. Craig, "Euler-bernoulli beam theory," in *Structural analysis*. Springer, 2009, pp. 173–221.

[24] D. Pan, Y. Shen, C. Huang, and Z. Wu, "Analysis of snap-through behavior of bistable buckled beam under end-moment static actuation," *International Journal of Non-Linear Mechanics*, vol. 142, p. 103937, 2022. [Online]. Available: https://www.sciencedirect.com/science/article/pii/S0020746222000208

[25] Dassault Systèmes. (2021) Abaqus/cae. Version 2021. [Online]. Available: https://www.3ds.com/products-services/simulia/products/abaqus/

[26] D. Lees and G. Chirikjian, "A combinatorial approach to trajectory planning for binary manipulators," in *Proceedings of IEEE International Conference on Robotics and Automation*, vol. 3, 1996, pp. 2749–2754 vol.3.

[27] I. Ebert-Uphoff and G. Chirikjian, "Inverse kinematics of discretely actuated hyper-redundant manipulators using workspace densities," in *Proceedings of IEEE International Conference on Robotics and Automation*, vol. 1, 1996, pp. 139–145 vol.1.

[28] J. Wang and E. Olson, "Apriltag 2: Efficient and robust fiducial detection," in *2016 IEEE/RSJ International Conference on Intelligent Robots and Systems (IROS)*. IEEE, 2016, pp. 4193–4198.